Quantifying Energy Balance Regimes in the Modern Climate, Their Link to Lapse Rate Regimes, and Their Response to Warming

OSAMU MIYAWAKI,[a] TIFFANY A. SHAW,[a] AND MALTE F. JANSEN[a]

[a] *The University of Chicago, Chicago, Illinois*

(Manuscript received 7 June 2021, in final form 12 October 2021)

ABSTRACT: Energy balance and lapse rate regimes qualitatively characterize the low, middle, and high latitudes of Earth's modern climate. Currently we do not have a complete quantitative understanding of the spatiotemporal structure of energy balance regimes [e.g., radiative convective equilibrium (RCE) and radiative advective equilibrium (RAE)] and their connection to lapse rate regimes (moist adiabat and surface inversion). Here we use the vertically integrated moist static energy budget to define a nondimensional number that quantifies where and when RCE and RAE are approximately satisfied in Earth's modern climate. We find RCE exists year-round in the tropics and in the northern midlatitudes during summertime. RAE exists year-round over Antarctica and in the Arctic with the exception of early summer. We show that lapse rates in RCE and RAE are consistent with moist adiabatic and surface inversion lapse rates, respectively. We use idealized models (energy balance and aquaplanet) to test the following hypotheses: 1) RCE occurs during midlatitude summer for land-like (small heat capacity) surface conditions, and 2) sea ice is necessary for the existence of annual-mean RAE over a polar ocean, such as the Arctic. Consistent with point 1, an aquaplanet configured with a shallow mixed layer transitions to RCE in the midlatitudes during summertime whereas it does not for a deep mixed layer. Furthermore, we confirm point 2 using mechanism-denial aquaplanet experiments with and without thermodynamic sea ice. Finally, we show energy balance regimes of the modern climate provide a useful guide to the vertical structure of the warming response in the annual mean, and seasonally over the tropics and the southern high latitudes.

KEYWORDS: Sea ice; Inversions; Energy budget/balance; Stability; Temperature; Seasonal cycle

1. Introduction

Earth's modern climate is maintained by three types of energy transfer: advection, radiation, and surface turbulent fluxes (e.g., see Hartmann 2016, ch. 6.2). These energy transfer types can be most easily defined using the vertically integrated, zonal-mean, annual-mean moist static energy (MSE) budget:

$$\underbrace{\langle \partial_y \overline{[vm]} \rangle}_{\text{advection}} = \underbrace{\overline{[R_a]}}_{\text{radiation}} + \underbrace{\overline{[\text{LH}]} + \overline{[\text{SH}]}}_{\text{surface turbulence}}, \tag{1}$$

where $m = c_p T + gz + Lq$ is MSE, $\overline{(\cdot)}$ is the annual mean, $[\cdot]$ is the zonal mean, and $\langle \cdot \rangle$ is the mass-weighted vertical integral (Neelin and Held 1987). Advection corresponds to the meridional divergence—$\partial_y(\cdot) \equiv (1/r\cos\phi)\partial_\phi[(\cdot)\cos\phi]$ is the meridional divergence in spherical coordinates, where ϕ is latitude and r is the radius of Earth—of MSE flux (vm where v is meridional velocity) and represents the energy transported by the atmospheric circulation, such as the Hadley cell and storm tracks. Radiation R_a corresponds to atmospheric radiative cooling, which is the difference of the top of atmosphere and surface radiative fluxes. Finally, surface turbulent fluxes correspond to surface latent heat (LH) and sensible heat (SH) flux.

In the annual mean, the dominant types of energy transfer depend on latitude (e.g., see Fig. 6.1 in Hartmann 2016). In the low latitudes, atmospheric radiative cooling is primarily balanced by surface turbulent fluxes (Riehl and Malkus 1958), which destabilize the column to convection by supplying moist, warm air to the boundary layer. The dominant balance between radiative cooling and surface turbulent fluxes is consistent with radiative convective equilibrium (RCE; Wing et al. 2018). In the high latitudes, atmospheric radiative cooling is primarily balanced by advection from lower latitudes (Nakamura and Oort 1988) consistent with radiative advective equilibrium (RAE; Cronin and Jansen 2016). Finally in the midlatitudes, all three types of energy transfer are important; thus, we introduce the term radiative convective advective equilibrium (RCAE). In this way, three energy balance regimes qualitatively characterize the low-, mid-, and high-latitude regions of Earth's modern climate.

Annual mean lapse rate regimes also qualitatively characterize the low-, mid-, and high-latitude regions of Earth's modern climate. The low latitudes exhibit a moist adiabatic lapse rate regime (Stone and Carlson 1979; Betts 1982; Xu and Emanuel 1989; Williams and Renno 1993). The high latitudes exhibit a surface inversion lapse rate regime (e.g., see Fig. 1.3 in Hartmann 2016). Finally, the midlatitudes are a mixed regime, which is more stable than a moist adiabat (Stone and Carlson 1979; Korty and Schneider 2007) with no surface inversion.

The lapse rate regime varies through the seasonal cycle in the Northern Hemisphere. For example, the midlatitudes exhibit a moist adiabatic regime in summer and a mixed regime in winter (Stone and Carlson 1979). The Northern Hemisphere high latitudes exhibit a mixed regime in summer and a surface inversion regime in winter (Bradley et al. 1992; Tjernström and Graversen 2009; Devasthale et al. 2010; Zhang et al. 2011; Cronin and Jansen 2016).

Denotes content that is immediately available upon publication as open access.

Corresponding author: Osamu Miyawaki, miyawaki@uchicago.edu

DOI: 10.1175/JCLI-D-21-0440.1

While energy balance and lapse rate regimes qualitatively characterize the low, middle, and high latitudes of Earth's modern climate, few studies to date have quantified the latitudinal and seasonal dependence of observed energy balance regimes and their link to lapse rate regimes in reanalyses and general circulation models (GCMs).

Quantifying the latitudinal and seasonal dependence of observed energy balance regimes would allow us to assess where and when idealized models that assume RCE or RAE hold. This would be useful for several reasons. First, the results of many studies investigating the tropical climate (precipitation, cloud, and circulation) and its response to warming use models that assume RCE (e.g., Romps 2011; Popke et al. 2013; Pendergrass et al. 2016; Merlis and Held 2019). Quantifying the latitudinal and seasonal dependence of RCE in the modern climate can guide where and when these insights are applicable. Jakob et al. (2019) took a first step in this direction by quantifying the spatial and temporal scales that satisfy RCE in the tropics. However, they did not examine the possible occurrence of RCE outside of the tropics or energy balance regimes more generally (RAE and RCAE).

Second, knowledge of energy balance regimes for the modern climate could provide a useful guide for interpreting the vertical structure of the warming response latitudinally and seasonally. For regions that are in RCE in the modern climate and remain in RCE in the future, the expectation is that warming maximizes aloft (Held 1993; Romps 2011). For regions that are in RAE in the modern climate and remain in RAE in the future, the expectation is that warming maximizes at the surface (assuming that the radiative forcing dominates over changes in surface or advective heat flux; Held 1993; Cronin and Jansen 2016). However, it is an open question whether energy balance regimes in the modern climate provide a useful guide to the vertical structure of the warming response latitudinally and seasonally.

Here we seek to answer the following questions. Where and when do energy balance regimes (RCE, RAE, and RCAE) occur in Earth's modern climate? How closely are they linked to lapse rate regimes (moist adiabatic, surface inversion, and mixed)? Do energy balance regimes in the modern climate provide a useful guide for interpreting the vertical structure of the warming response? To answer these questions, we develop a nondimensional number based on the MSE budget to quantify energy balance regimes (section 2a). We use this nondimensional number to quantify where and when energy balance regimes occur latitudinally and seasonally in Earth's modern climate using reanalysis and Coupled Model Intercomparison Project phase 5 (CMIP5) data. We quantify the connection between energy balance and lapse rate regimes (section 3) and use idealized climate models to formulate and test hypotheses that explain the seasonality of energy balance regime transitions in the Northern Hemisphere (section 4). Finally, we investigate whether energy balance regimes in the modern climate are a useful guide to the vertical structure of the warming response in CMIP5 models (section 5). The results are summarized and discussed in section 6.

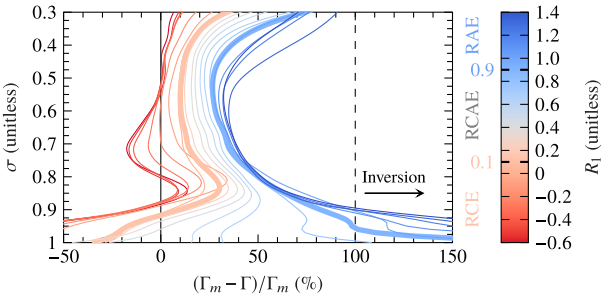

FIG. 1. The zonal-mean, annual-mean percent deviation of the lapse rate from the moist adiabatic lapse rate binned by R_1 (bin widths are 0.1) for the reanalysis mean. Thick blue and orange lines correspond to $R_1 = 0.9$ and $R_1 = 0.1$, respectively. A 100% deviation from the moist adiabat denotes an isothermal atmosphere and hence marks the threshold for an inversion.

2. Methods

a. *Defining energy balance regimes using the nondimensionalized MSE budget*

To define energy balance regimes seasonally, we begin with the vertically integrated, zonal-mean MSE equation:

$$\langle [\partial_t m] \rangle + \langle [\partial_y vm] \rangle = [R_a] + [\mathrm{LH}] + [\mathrm{SH}] \,, \tag{2}$$

where $\langle [\partial_t m] \rangle$ represents atmospheric MSE storage. To nondimensionalize Eq. (2), we divide by radiative cooling R_a, which is sign definite for the modern climate:

$$\underbrace{\frac{\partial_t m + \partial_y (vm)}{R_a}}_{R_1} = 1 + \underbrace{\frac{\mathrm{LH} + \mathrm{SH}}{R_a}}_{R_2} \,, \tag{3}$$

where R_1 and R_2 are nondimensional numbers and the $[\cdot]$ and $\langle \cdot \rangle$ notations have been dropped for brevity.

In the strictest sense, RCE is a steady-state equilibrium where radiation balances surface turbulent fluxes ($R_1 = 0$). As this is exactly satisfied only in the global mean, we define RCE as $R_1 \leq \varepsilon$, where ε is a small number. This definition includes regions of vertically integrated MSE flux divergence and weak convergence because temperature profiles in regions of divergence are set by convective adjustment (Warren et al. 2020).

RAE as defined in Cronin and Jansen (2016) requires surface turbulent fluxes to be negligibly small ($R_2 = 0$ or equivalently $R_2 = 1$). Although exact RAE further requires atmospheric storage to be small ($\partial_t m = 0$), the framework developed by Cronin and Jansen (2016) could readily be generalized to account for the time tendency term, which would add to the advective tendency. To be consistent with the definition of RCE, we define RAE as regions where surface turbulent fluxes are small or directed from the atmosphere to the surface ($R_2 \geq -\varepsilon$ or equivalently $R_1 \geq 1 - \varepsilon$).

To choose the value for ε, we examine the deviation of the zonal-mean, annual-mean lapse rate from the moist adiabatic lapse rate binned by the value of R_1 using reanalysis data (Fig. 1). The lapse rate deviation is plotted in sigma coordinates

to ensure that surface inversions are properly represented (see appendix A for more details). The tropospheric lapse rate deviation is nearly a monotonic function of R_1 (especially above $\sigma = 0.7$ and below $\sigma = 0.9$), demonstrating the quantitative link between energy balance and lapse rate regimes. The surface inversion lapse rate regime occurs for $R_1 \geq 0.9$ and thus we define the RAE regime as $R_1 \geq 1 - \varepsilon = 0.9$ (thick blue line, Fig. 1). Consistently, we define the RCE regime as $R_1 \leq \varepsilon = 0.1$. Where $R_1 \leq 0.1$, the free tropospheric lapse rate (vertically averaged from $\sigma = 0.7$ to 0.3) is in the moist adiabatic lapse rate regime (i.e., it deviates from the moist adiabatic lapse rate by less than 13%; thick orange line in Fig. 1). Finally, we define the RCAE regime as where $0.1 < R_1 < 0.9$, where it corresponds to the mixed lapse rate regime (i.e., >13% more stable than a moist adiabatic lapse rate but does not exhibit a surface inversion).

b. Reanalysis data

We consider three reanalysis datasets from 1980 through 2005: ERA5 (Hersbach et al. 2020), MERRA-2 (Gelaro et al. 2017), and JRA-55 (Kobayashi et al. 2015). We focus on the energy balance and lapse rate regimes for the multi-reanalysis mean and show the spread as the range across the three reanalyses. Atmospheric storage ($\partial_t m$) is computed by taking the finite difference of MSE using monthly temperature, specific humidity, and geopotential data, following Donohoe et al. (2013). Additionally, we use the monthly radiative (R_a) and surface turbulent (LH and SH) fluxes and infer the advective flux [$\partial_y(vm)$] as the residual. We choose to infer advection as the residual because the mass-correction technique for directly computing the MSE flux divergence in reanalysis data is known to produce unphysical results in the high latitudes (Porter et al. 2010).

c. CMIP5 simulations

We consider the r1i1p1 historical simulation averaged over 1980–2005 and the r1i1p1 RCP8.5 simulation averaged over 2070–99 for 36 CMIP5 models (Taylor et al. 2012; also see Table B1 in appendix B herein). We show the energy balance and lapse rate regimes for the multimodel mean and show the spread as the interquartile range across the models. Consistent with the reanalysis products, we compute R_1 using monthly $\partial_t m$, R_a, LH, and SH, and infer $\partial_y(vm)$ as the residual.

d. Idealized climate models

We use two idealized climate models to understand the seasonal changes in energy balance regimes. At intermediate complexity, we examine seasonal changes in the ECHAM6 slab ocean aquaplanet model (Stevens et al. 2013), hereafter referred to as AQUA. AQUA simulations are configured with a seasonal cycle, no ocean heat transport, modern greenhouse gas concentrations, and with or without thermodynamic sea ice following Shaw and Graham (2020). Details of the thermodynamic sea ice model in ECHAM6 are provided in Giorgetta et al. (2013).

To explore the seasonal variation in energy balance regimes, we vary the mixed layer depth in AQUA from 3 to 50 m without sea ice and from 25 to 50 m with ice, following previous work (Donohoe et al. 2014; Barpanda and Shaw 2020; Shaw and Graham 2020). Shaw and Graham (2020) showed that AQUA enters a Snowball Earth regime for mixed layer depths below 20 m; hence, 25 m is the minimum mixed layer depth for AQUA with ice considered here. A monthly climatology is obtained by averaging the last 20 years of the 40-yr simulation except for the 3-m configuration, where the last 5 years of a 15-yr simulation are averaged due to the faster equilibration. Consistent with the reanalysis products and the CMIP5 simulations, we compute R_1 using the monthly $\partial_t m$, R_a, LH, and SH, and infer $\partial_y(vm)$ as the residual.

At the simple end, we use the energy balance model (EBM) of Rose et al. (2017). The EBM is an equation for the zonal-mean surface temperature:

$$\rho c_w d\, \partial_t T_s = aQ - (A + BT_s) + \frac{D}{\cos\phi}\partial_\phi(\partial_\phi T_s \cos\phi)\,, \qquad (4)$$

where ρ is the density of water, c_w is the specific heat capacity of liquid water, d is the mixed layer depth, T_s is the zonal-mean surface temperature, a is the coalbedo, Q is insolation, $A + BT_s$ is outgoing longwave radiation where A and B are constant coefficients, ϕ is latitude, and D is the diffusivity, which is assumed to be a constant. We set $A = -410$ W m^{-2}, $B = 2.33$ W m^{-2} K^{-1}, $D = 0.90$ W m^{-2} K^{-1}, and $a = 0.72$, which are obtained from best fits to AQUA configured with a 25-m mixed layer depth and without sea ice. Best fits of A and B are obtained by taking the least squares linear regression of the zonal-mean OLR and T_s. The best fit of D is obtained similarly by taking the least squares linear regression of $\partial_y(vm)$ and $(1/\cos\phi)\partial_\phi(\partial_\phi T_s \cos\phi)$ for latitudes poleward of 25°. Last, a is computed as the globally averaged diagnosed planetary coalbedo.

3. Energy balance regimes in reanalysis data

a. Annual-mean energy balance regimes

In the annual mean, the RCE regime, defined by $R_1 \leq 0.1$, extends from the deep tropics to ~40° (black line overlapping orange region in Fig. 2a). The moist adiabatic lapse rate regime occurs in the same region. In particular, the free tropospheric lapse rate, defined as the vertically averaged lapse rate from $\sigma = 0.7$ to 0.3, closely follows R_1 (cf. orange and black lines in Fig. 2a) and deviates from −3% to + 13% from a moist adiabat where $R_1 \leq 0.1$.

The RAE regime, defined by $R_1 \geq 0.9$, occurs poleward of ~80°N and ~70°S in the annual mean (black line overlapping blue region in Fig. 2b). The reanalysis spread in the high latitudes is large in both hemispheres due to high uncertainty in the estimation of surface turbulent fluxes (Tastula et al. 2013; Graham et al. 2019). The largest values of R_1 are found over Antarctica whereas R_1 is close to the RCAE threshold in the Arctic. The RAE regime coincides with a surface inversion lapse rate regime. Specifically, the region where $R_1 \geq 0.9$ exhibits >100% deviation from a moist adiabat indicating a surface inversion (blue line in Fig. 2b).

Last, the RCAE regime, defined by $0.1 < R_1 < 0.9$, occurs between 40°–80°N and 40°–70°S in the annual mean (black

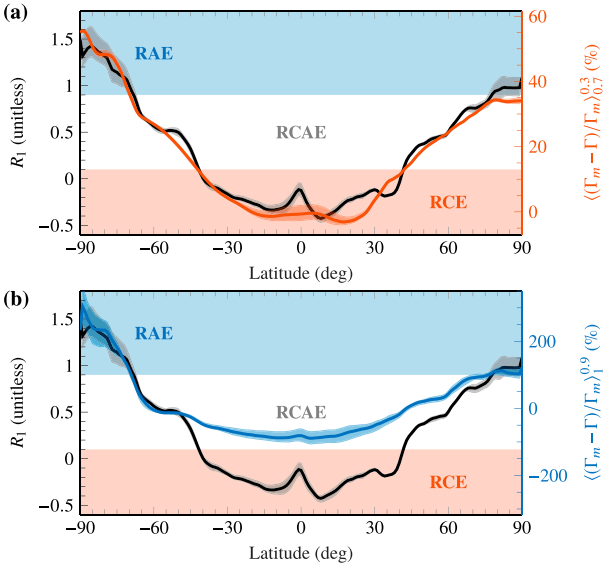

FIG. 2. (a) The zonal-mean, annual-mean structure of R_1 (black line, left axis) and the vertically averaged free tropospheric (σ = 0.7–0.3) lapse rate deviation from the moist adiabatic lapse rate (orange line, right axis) for the reanalysis mean. Orange, white, and blue regions indicate RCE, RCAE, and RAE, respectively. (b) The zonal-mean, annual-mean structure of R_1 (black line, left axis) and the vertically averaged boundary layer (σ = 1–0.9) lapse rate deviation from the moist adiabatic lapse rate (blue line, right axis) for the reanalysis mean. The shading over the lines indicates the range across the reanalyses.

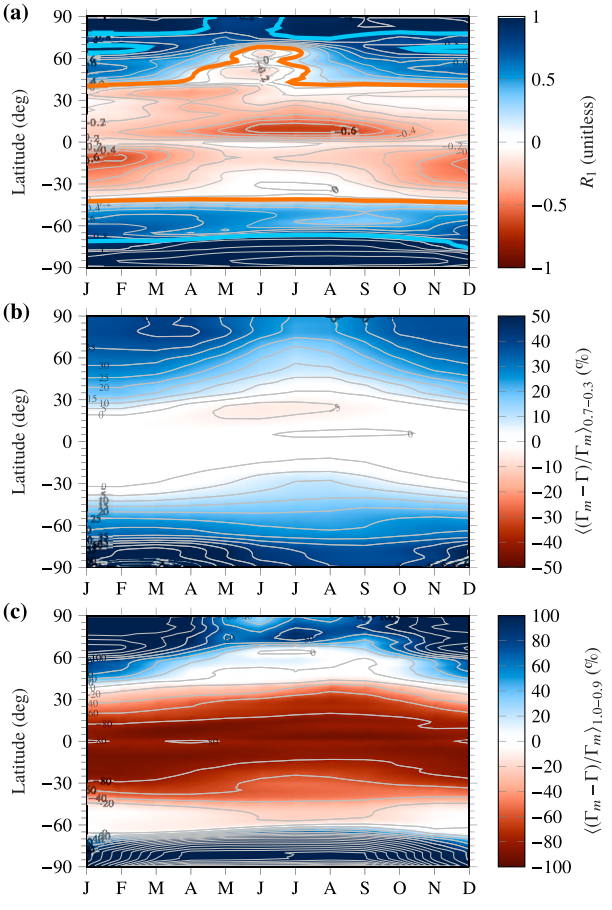

FIG. 3. (a) The seasonality of R_1 (contour interval is 0.1) for the reanalysis mean. The thick orange contour indicates the RCE/RCAE boundary (R_1 = 0.1), and the thick blue contour indicates the RAE/RCAE boundary (R_1 = 0.9). (b) The spatiotemporal structure of the free tropospheric (vertically averaged from σ = 0.7 to 0.3) lapse rate deviation from a moist adiabat for the reanalysis mean (contour interval is 5%). (c) The spatiotemporal structure of the boundary layer (vertically averaged from σ = 1 to 0.9) lapse rate deviation from the moist adiabatic lapse rate for the reanalysis mean (contour interval is 20%).

line overlapping the white region in Fig. 2a). The RCAE regime coincides with the mixed lapse rate regime, where the lapse rate is more stable than a moist adiabat and does not exhibit a surface inversion. Specifically, the free tropospheric lapse rate in the region where $0.1 < R_1 < 0.9$ deviates from + 13% to + 35% from a moist adiabat.

b. *Seasonality of energy balance regimes*

The seasonality of R_1 is weak in the Southern Hemisphere, such that the latitudinal extent of RCE (equatorward of 40°S), RAE (poleward of 70°S), and RCAE regimes (between 40° and 70°S) is largely the same throughout the year (Fig. 3a). Consistently, the midlatitudes exhibit a mixed lapse rate regime (Fig. 3b) and the high latitudes exhibit a surface inversion year-round (Fig. 3c)

In the Northern Hemisphere, the RCE regime occurs year-round equatorward of 40°N and expands poleward to 70°N during June (region equatorward of the thick orange contour in Fig. 3a). The seasonality of the moist adiabatic lapse rate regime similarly expands poleward during summertime (e.g., see the 15% deviation contour in Fig. 3b). However, there is a phase shift between the seasonality of energy balance and lapse rate regimes in the midlatitudes. The northern midlatitudes are in the RCE regime from April to July but in the moist adiabatic lapse rate regime from June to September (cf. solid black and orange lines in Fig. 4a). This lag is associated with the seasonality of atmospheric storage. When atmospheric storage is excluded from R_1, there is closer agreement in the phase of the energy balance and lapse rate seasonality (cf. dashed black and orange lines in Fig. 4a).

The Northern Hemisphere RAE regime occurs poleward of 80°N with the exception of May and June (region poleward of the thick blue contour in Fig. 3a). Consistently, the mixed lapse rate regime occurs during May and June (Fig. 3c) but persists through September despite being in a state of RAE (cf. solid black and blue lines in Fig. 4b). The atmospheric storage term again plays an important role in the seasonal atmospheric MSE budget (cf. solid and dashed black lines in Fig. 4b). However, unlike in the midlatitudes, the discrepancy in the timing of the energy balance and lapse rate regimes in the high latitudes cannot be directly related to the seasonality of atmospheric storage (cf. dashed black and blue lines in Fig. 4b).

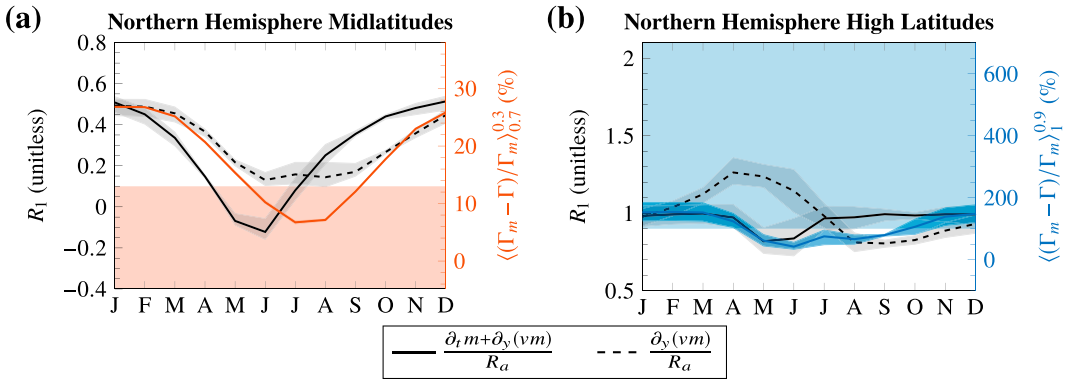

FIG. 4. The seasonality of R_1 with (solid black) and without (dashed black) atmospheric storage is compared to the lapse rate seasonality in the free troposphere (orange line) and near the surface (blue line) for the Northern Hemisphere (a) midlatitudes (40°–60°N) and (b) high latitudes (80°–90°N) for the reanalysis mean. The shading over the lines indicates the range across the reanalyses. The orange and blue regions indicate RCE and RAE regimes, respectively.

c. *Decomposition of seasonal energy balance regime transitions*

To diagnose the physical mechanism responsible for the seasonal energy balance regime transitions in the Northern Hemisphere, we decompose the seasonality of R_1 as follows:

$$\Delta R_1 = \overline{R_1}\left\{\frac{\Delta\left[\partial_t m + \partial_y(vm)\right]}{\overline{\partial_t m + \partial_y(vm)}} - \frac{\Delta R_a}{\overline{R_a}}\right\} + \text{Residual}\,, \tag{5}$$

where $\Delta(\cdot)$ is the deviation from the annual mean and $\overline{(\cdot)}$ is the annual mean. The dynamic component [first term on the right-hand side of Eq. (5)] quantifies the importance of advection plus atmospheric storage, and the radiative component [second term on the right-hand side of Eq. (5)] quantifies the importance of radiative cooling. Last, the residual quantifies the importance of nonlinear interactions.

The RCAE to RCE regime transition in the northern midlatitudes (where the solid black line intersects the orange region in Fig. 5a) closely follows the dynamic component (cf. black and red lines in Fig. 5a) whereas the other terms are small (gray and dash-dotted line in Fig. 5a). The RCE regime corresponds to the time when advection plus atmospheric storage is small (sum of black and red lines in Fig. 5b). In the Southern Hemisphere, the dynamic and radiative components are of similar magnitude and partially compensate, leading to relatively small seasonality in R_1 (Fig. 5c). The radiative components are similar between the two hemispheres (cf. gray lines in Figs. 5a, c). Thus, there is no midlatitude regime transition to RCE in the Southern Hemisphere because the dynamic component is small, which is consistent with the small seasonality of advection plus storage (black and red lines in Fig. 5d).

The RAE to RCAE regime transition in the northern high latitudes is the outcome of opposing dynamic and radiative components (Fig. 6a). Since $\overline{R_1} = \overline{\partial_t m + \partial_y(vm)}/\overline{R_a} \approx 1$ in the northern high latitudes (see black line in Fig. 2), Eq. (5) simplifies to

$$\Delta R_1 \approx \frac{1}{\overline{R_a}}\left\{\Delta\left[\partial_t m + \partial_y(vm)\right] - \Delta R_a\right\} + \text{Residual} \tag{6}$$

$$= \frac{1}{\overline{R_a}}\Delta(\text{LH} + \text{SH}) + \text{Residual}\,, \tag{7}$$

where we have used the MSE budget [Eq. (2)]. Thus, the regime transition in the northern high latitudes is connected to the seasonality of surface turbulent fluxes, which is dominated by an increase in latent heat flux from May to September (blue line, Fig. 6b).

In the southern high latitudes, the seasonality of surface turbulent fluxes and thus ΔR_1 is comparable to that of the northern high latitudes (cf. Figs. 6a,b and 6c,d). However, there is no regime transition in the southern high latitudes because annual-mean R_1 is farther from the regime transition threshold for RAE ($\overline{R_1} = 1.36$). The larger annual-mean R_1 is associated with smaller radiative cooling and a persistent downward sensible heat flux (gray and orange lines in Fig. 6d).

While the results above focused on the reanalysis mean, similar seasonality is found in the CMIP5 historical simulations (Figs. B1–B6). In particular, CMIP5 models capture the regime transition in the northern midlatitudes and its connection to the large seasonality of advection plus storage (Fig. B5). CMIP5 models also capture the regime transition in the northern high latitudes and its connection to a summertime increase in latent heat flux (Fig. B6). Some small differences between the reanalysis and CMIP5 mean are discussed in appendix B.

4. Testing hypotheses to explain seasonal energy balance regime transitions

a. *Midlatitude regime transition*

Previous studies have found that surface heat capacity controls the seasonality of various climate phenomena, such as

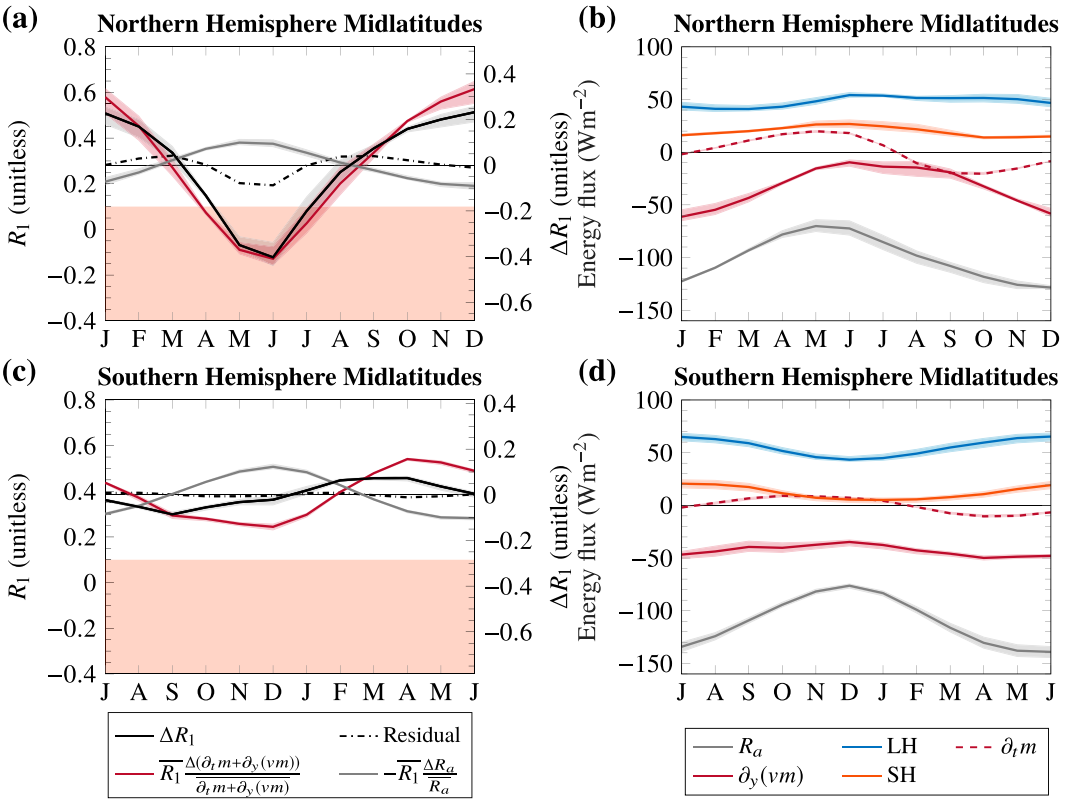

FIG. 5. The seasonality of R_1 in the midlatitudes (40°–60°, thick black line, left axis) and its deviation from the annual mean (horizontal black line), ΔR_1 (right axis), are shown for the (a) Northern and (c) Southern Hemisphere for the reanalysis mean. The orange shading indicates the RCE regime. Here, ΔR_1 is decomposed into the dynamic (red line) and radiative (gray line) components according to Eq. (5). The seasonality of the MSE budget terms in the midlatitudes are shown for the (b) Northern and (d) Southern Hemisphere. The shading over the lines indicates the range across the reanalyses.

surface temperature (Donohoe et al. 2014), intertropical convergence zone (Bordoni and Schneider 2008), and storm track intensity and position (Barpanda and Shaw 2020), due to its effect on the seasonality of surface energy fluxes. Thus, we hypothesize that surface heat capacity controls the existence of midlatitude energy balance regime transitions. To connect the seasonality of R_1 to surface heat capacity, we begin by rewriting the atmospheric MSE budget in terms of top of the atmosphere (F_{TOA}) and surface (F_{SFC}) fluxes following Barpanda and Shaw (2020):

$$\Delta\left[\partial_t m + \partial_y(vm)\right] = \Delta F_{\mathrm{TOA}} - \Delta F_{\mathrm{SFC}}\,. \tag{8}$$

We can write the seasonality of surface fluxes using the surface energy budget of a mixed layer ocean:

$$\Delta F_{\mathrm{SFC}} = \rho c_w d\Delta(\partial_t T_s) + \Delta(\partial_y F_O) \approx \rho c_w d\Delta(\partial_t T_s)\,, \tag{9}$$

where ρ is the density of water, c_w is the specific heat capacity of liquid water, d is the mixed layer depth, and $\Delta(\partial_y F_O)$ is the seasonality of meridional ocean heat flux divergence, which we neglect because it is small (Roberts et al. 2017). Finally, we divide by $\overline{R_a}$ and combine Eqs. (5), (8), and (9) to obtain an equation for the seasonality of R_1:

$$\Delta R_1 \approx \frac{\Delta\left[\partial_t m + \partial_y(vm)\right]}{\overline{R_a}} = \frac{1}{\overline{R_a}}\left[\Delta F_{\mathrm{TOA}} - \rho c_w d\Delta(\partial_t T_s)\right], \tag{10}$$

where the radiative component is assumed to be negligible, consistent with the northern midlatitudes where the regime transition occurs (see Fig. 5a). To close Eq. (10), which depends on the unknown surface temperature tendency, we make use of the EBM (see section 2d and appendix C for more details). Using the analytic EBM, Eq. (10) becomes

$$\Delta R_1 = \frac{Q^*}{\overline{R_a}}\frac{2D}{(B+2D)^2 + (\rho c_w d\omega)^2}\left[(B+2D)\cos(\omega t) + \rho c_w d\omega \sin(\omega t)\right], \tag{11}$$

where Q^* is the seasonal amplitude of insolation and $\omega = 2\pi$ yr^{-1}. Thus, the EBM predicts that the seasonality of R_1 is large for shallow mixed layer depths and small for deep mixed layer depths (black line, Fig. 7a)

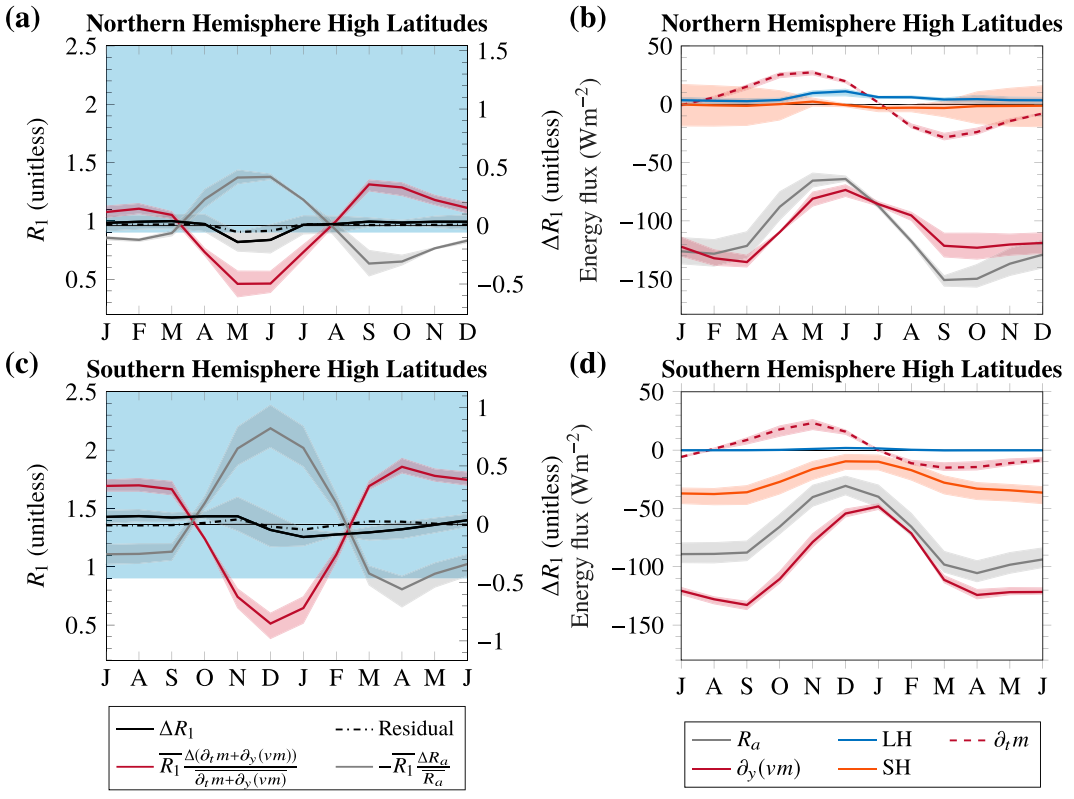

FIG. 6. As in Fig. 5, but averaged over the high latitudes (80°–90°).

The dependence of the amplitude of ΔR_1 on mixed layer depth in AQUA is qualitatively consistent with the EBM prediction (cf. stars to solid black line in Fig. 7a). Both AQUA and EBM agree that the midlatitude regime transition from RCAE to RCE only occurs for shallow mixed layer depths. The regime transition occurs in the EBM for $d \leq 16$ m and in AQUA for $d \leq 20$ m (intersection of the line and stars with the orange region in Fig. 7a). This is consistent with the observed hemispheric asymmetry in the midlatitude regime transition. The regime transition is absent in the ocean-dominated (deep mixed layer) southern midlatitudes (Fig. 5c) whereas the regime transition occurs in the northern midlatitudes (Fig. 5a), where the land fraction is higher (shallower mixed layer depth).

The phase of R_1 is also a function of the mixed layer depth in AQUA (Fig. 7b). The seasonal minimum of R_1 occurs as early as June in AQUA with a 3-m mixed layer depth and as late as September with a 50-m mixed layer depth. While

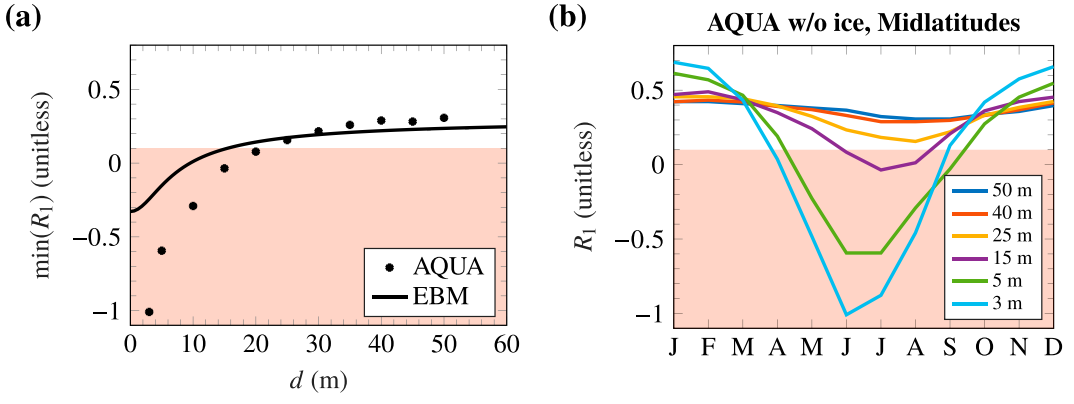

FIG. 7. (a) Midlatitude (40°–60°) R_1 seasonality measured by the minimum value of R_1 predicted by the EBM (solid black line) and simulated by AQUA (stars). (b) Seasonality of midlatitude (40°–60°) R_1 for various mixed layer depths in AQUA without sea ice. The orange region denotes the RCE regime.

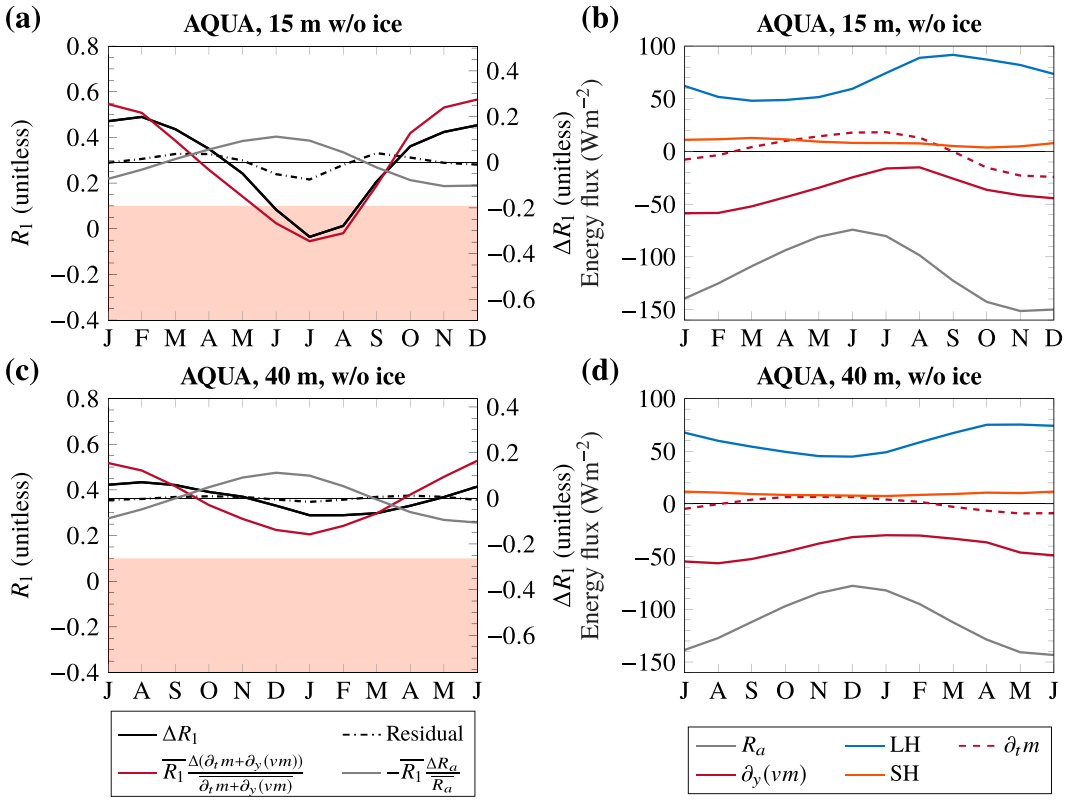

FIG. 8. As in Fig. 5, but for AQUA without sea ice for (a),(b) 15- and (c),(d) 40-m mixed layer depth.

AQUA with a 3-m mixed layer depth captures the phase of R_1 in the northern midlatitudes in reanalysis data, it overpredicts the amplitude by a factor of 3 (cf. cyan line in Fig. 7b with black line in Fig. 5a). This suggests that the seasonality in the Northern Hemisphere may be the result of zonal variations in surface heat capacity (land vs ocean).

When AQUA is configured with a mixed layer depth of 15 m, the amplitude of the R_1 seasonality closely resembles the northern midlatitudes (cf. Fig. 8a and Fig. 5a). However, the regime transition in AQUA with a 15-m mixed layer depth lags that in reanalysis data as discussed above. The regime transition in AQUA is associated with a large seasonality of advection plus atmospheric storage, consistent with the northern midlatitudes in reanalysis data (cf. Figs. 8b and 5b).

When AQUA is configured with a 40-m mixed layer depth, ΔR_1 closely resembles the southern midlatitudes; namely, there is no regime transition (cf. Figs. 8c and 5c). The persistence of the RCAE regime throughout the seasonal cycle in the 40-m aquaplanet simulation can be attributed to the weak seasonality of advection plus atmospheric storage, consistent with the results for the southern midlatitudes in reanalysis data (cf. Figs. 8d and 5d).

b. *High-latitude regime transition*

The polar regions on Earth are fundamentally different in that the Northern Hemisphere has a polar ocean whereas the Southern Hemisphere has a polar continent. Given these differences, we quantify the importance of the following mechanisms for the energy balance regime seasonality in the high latitudes: 1) sea ice in the Arctic and 2) topography in the Antarctic.

Sea ice in the Arctic affects the surface heat capacity, surface albedo, and surface turbulent fluxes (Andreas et al. 1979; Maykut 1982). We therefore expect sea ice to play a key role in the seasonality of energy balance regimes in the northern high latitudes. We test the importance of sea ice using mechanism-denial experiments where AQUA is configured with and without thermodynamic sea ice for various mixed layer depths (section 2d).

Without sea ice, AQUA has a fixed surface albedo of the ocean (0.07) and in the annual mean, the high latitudes are in the RCAE and mixed lapse rate regime for all mixed layer depths (Table 1 and Figs. 9a,b). Thus, the low surface heat capacity effect of sea ice alone cannot account for the occurrence of annual-mean RAE in the northern high latitudes.

With sea ice, the annual-mean high latitudes in AQUA are in the RAE and surface inversion lapse rate regime for 25–40-m mixed layer depths (Table 1 and Figs. 9c,d). For deeper mixed layer depths, the high latitudes are in RCAE. Thus, sea ice is a necessary but not a sufficient condition for obtaining annual-mean RAE in the northern high latitudes.

Without sea ice, the high latitudes in AQUA do not exhibit a seasonal regime transition from RCAE to RAE across most mixed layer depths (10–50 m; see Fig. 9a). The exception is

TABLE 1. Annual-mean, high-latitude (80°–90°) R_1 and energy balance regimes for varied mixed layer depths (d) in AQUA with and without thermodynamic sea ice. The RAE regime is bolded for emphasis.

	d (m)	$\overline{R_1}$	Regime
AQUA without ice	5	0.74	RCAE
	10	0.80	RCAE
	15	0.79	RCAE
	25	0.76	RCAE
	40	0.77	RCAE
	50	0.76	RCAE
AQUA with ice	25	1.03	**RAE**
	30	0.95	**RAE**
	35	0.94	**RAE**
	40	0.94	**RAE**
	45	0.88	RCAE
	50	0.86	RCAE

the shallowest mixed layer depth (5 m), which exhibits a transition to RAE from March to May (Fig. 9a). However, the timing of the regime transition is not consistent with reanalysis data (Fig. 6a).

With sea ice, the high latitudes in AQUA exhibit a seasonal regime transition from RCAE to RAE across all mixed layer depths (25–50 m; Figs. 9c,d). For shallower mixed layer depths (25–40 m), the RAE and surface inversion regime occur from September to April (Figs. 9c,d). For deeper mixed layer depths (45 and 50 m), the RAE regime only occurs from December to April (Figs. 9c,d). The timing of energy balance and lapse rate regime transitions coincides in AQUA with ice (cf. Figs. 9c,d). In contrast, the timing of the energy balance and lapse rate regimes exhibit a discrepancy in the reanalysis data (Fig. 4b). The summertime energy balance regime transition in the reanalysis data is better represented by AQUA with shallower mixed layer depths (cf. solid black line in Fig. 4b and 25–40-m lines in Fig. 9c). On the other hand, the extended lapse rate regime transition in the reanalysis data is better represented by AQUA with deeper mixed layer depths (cf. blue line in Fig. 4b to 45- and 50-m lines in Fig. 9d).

The different timing of the seasonal RCAE to RAE regime transition in the high latitudes in AQUA with sea ice coincides with different sea ice fraction and depth during fall (Fig. 10). For shallower mixed layer depths (25–40 m), the high latitudes are in RAE in fall, which is associated with full coverage (Fig. 10b) of thick sea ice (Fig. 10c) and a high surface albedo (Fig. 10c). For deeper mixed layer depths (45 and

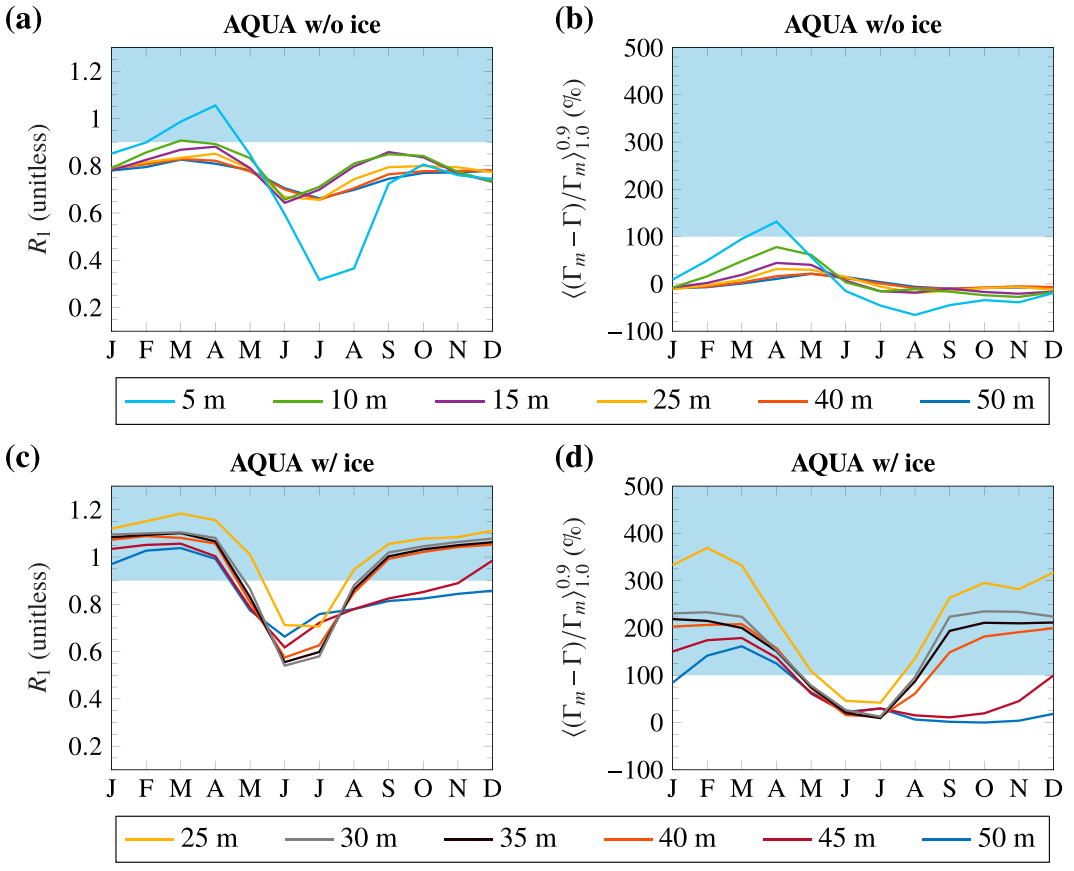

FIG. 9. (a) Seasonality of high-latitude (80°–90°) R_1 and (b) the boundary layer lapse rate deviation from a moist adiabat for various mixed layer depths in AQUA without sea ice. (c),(d) As in (a) and (b), but for AQUA with sea ice.

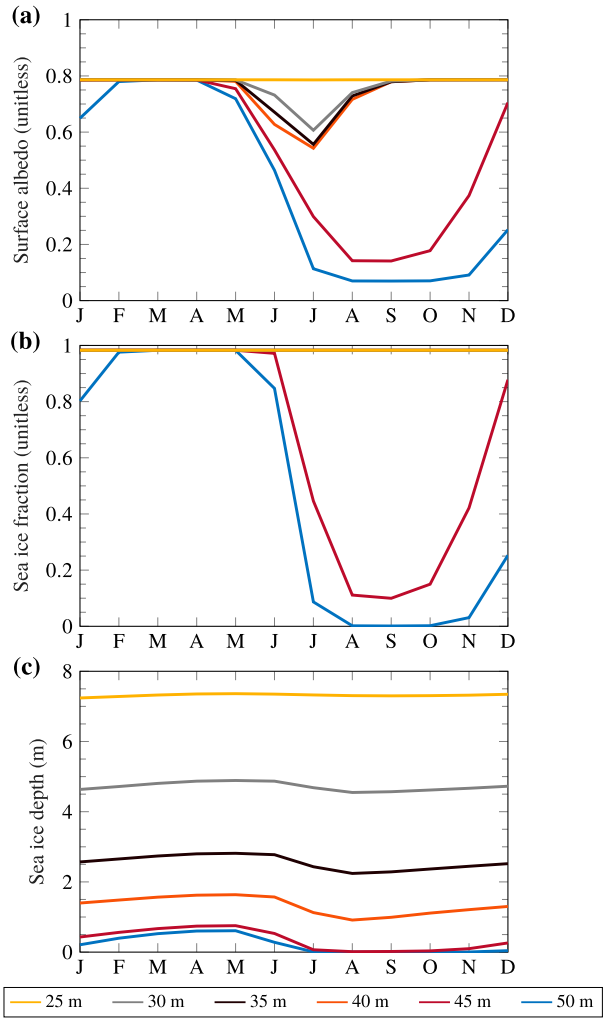

FIG. 10. Seasonality of high-latitude (80°–90°) (a) surface albedo, (b) sea ice fraction, and (c) sea ice depth for various mixed layer depths in AQUA with sea ice.

50 m), the high latitudes are in RCAE in the fall, which is associated with partial coverage (Fig. 10b) of thin sea ice (Fig. 10c) and lower albedo (Fig. 10a). These results suggest that sea ice impacts the timing of high latitude regime transitions through the combined effect of surface albedo and effective surface heat capacity, which themselves depend on the mixed layer depth in AQUA.

In the Antarctic, the annual-mean value of R_1 is larger than in the Arctic and there is no regime transition from RAE to RCAE. In the presence of Antarctic topography, the atmosphere is optically thinner, so that we expect atmospheric radiative cooling to be weaker (Jeevanjee and Romps 2018), and thus $R_1 = [\partial_t m + \partial_y(vm)]/R_a$ to be larger. We therefore investigate the impact of Antarctic topography on the seasonality of energy balance regimes using mechanism-denial experiments. In particular, we use the CESM simulations configured with and without Antarctic topography by Hahn et al. (2020).

The control CESM simulation with Antarctic topography captures the seasonality of R_1 in the reanalyses and CMIP5 historical runs. In particular, the northern high latitudes undergo a RAE to RCAE regime transition in June (solid line intersects the white region in Fig. 11a) while the southern high latitudes remain in RAE year-round (dashed line remains in the blue region in Fig. 11a). Without Antarctic topography, $\overline{R_1}$ decreases from 1.30 to 1.12 in the southern high latitudes (cf. Figs. 11a,b). However, because topography does not significantly affect summertime R_1, the southern high latitudes without Antarctic topography continue to remain in RAE year-round (dashed line remains in the blue region in Fig. 11b). Thus, while Antarctic topography partially explains the large hemispheric asymmetry in annual-mean R_1, it does not explain the lack of an energy balance regime transition in Antarctica.

The hemispheric asymmetry in energy balance regimes also cannot be solely explained by the near-constant high surface albedo in Antarctica, since an energy balance regime transition occurs in the presence of a seasonally invariant high surface albedo in AQUA (see 25-m simulation in Fig. 9c). Thus, multiple mechanisms may need to be considered together to understand the seasonality of energy balance regimes in Antarctica.

5. Connecting energy balance regimes in the modern climate to the vertical structure of the warming response

Here we quantify whether energy balance regimes in the modern climate provide a useful guide to the vertical, latitudinal, and seasonal structure of the warming response. For regions of RCE in the modern climate that stay in RCE in the future, the expectation is that warming maximizes aloft (Held 1993; Romps 2011). On the other hand, for regions of RAE in the modern climate that stay in RAE in the future, the expectation is that warming maximizes at the surface, assuming that the change in advective heat flux is negligible (Held 1993; Payne et al. 2015).

In the annual mean, the CMIP5 multimodel mean latitudinal structure of energy balance regimes remains unchanged by the end of the century with the exception of a small region between 75° and 80°N (cf. solid and dashed lines in Fig. 12a). Consistently, regions of RCE in the modern climate exhibit amplified warming aloft (red lines, $R_1 \leq 0.1$ in Fig. 12b) and regions of RAE in the modern climate exhibit amplified warming at the surface (blue lines, $R_1 \geq 0.9$ in Fig. 12b). Thus, energy balance regimes defined using R_1 in the modern climate can be used to interpret the vertical structure of the annual-mean warming response.

The seasonality of energy balance regimes in the tropics and southern high latitudes is largely unchanged in response to warming (cf. dashed and solid thick contours in Fig. 13). Consistently, the tropics, which are a region of RCE in the modern climate and stay in RCE in the future, exhibit amplified warming aloft throughout the seasonal cycle (red-filled contours in Fig. 13). Furthermore, the southern high latitudes, which are a region of RAE in the modern climate and stay in RAE in the future, exhibit amplified surface warming

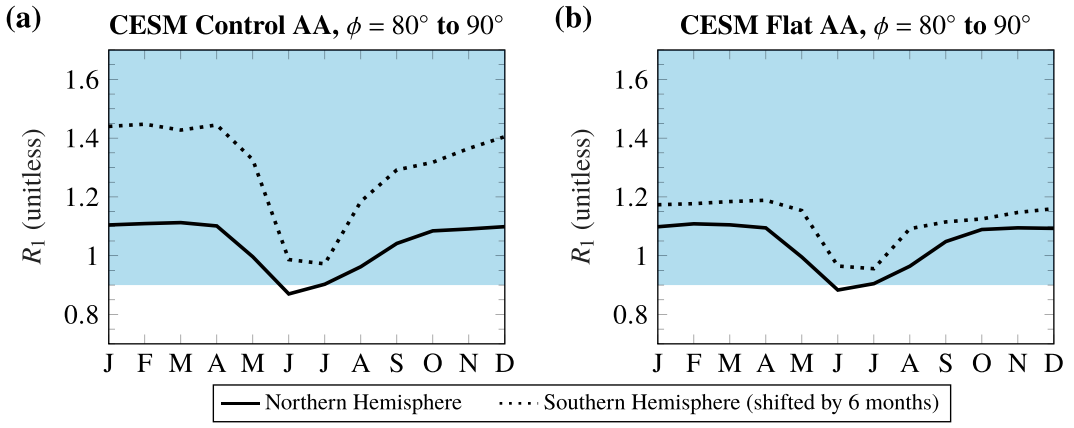

FIG. 11. Seasonality of R_1 in the CESM simulations performed by Hahn et al. (2020) in the northern (solid line) and southern (dotted line) high latitudes for the (a) control simulation with Antarctic topography and (b) flattened Antarctic topography simulation. The Southern Hemisphere seasonality is shifted by 6 months.

throughout the seasonal cycle (blue-filled contours in Fig. 13). Thus, energy balance regimes in the modern climate can also be used to interpret the vertical structure of the warming response seasonally in the tropics and southern high latitudes.

In the Northern Hemisphere middle and high latitudes, energy balance regimes in the modern climate are less directly related to the vertical structure of the warming response. In the Northern midlatitudes, there is a phase shift between the seasonality of energy balance regimes in the modern climate and the seasonality of the lapse rate change (cf. thick orange line to filled contours in Fig. 13). This discrepancy is similar to the phase shift between the seasonality of energy balance and lapse rate regimes in the modern climate (cf. Figs. 3a,b). This suggests that seasonal atmospheric heat storage may again be playing a role in delaying the seasonality of the lapse rate change relative to that of energy balance regimes.

The northern high latitudes exhibit significant changes in energy balance regimes in response to warming (cf. solid and dashed blue lines in Fig. 13), which coincide with significant changes in the advective heat flux into the Arctic, especially during summertime (not shown). Thus, the assumptions required for using energy balance regimes in the modern climate to interpret the warming response are not satisfied in the Arctic.

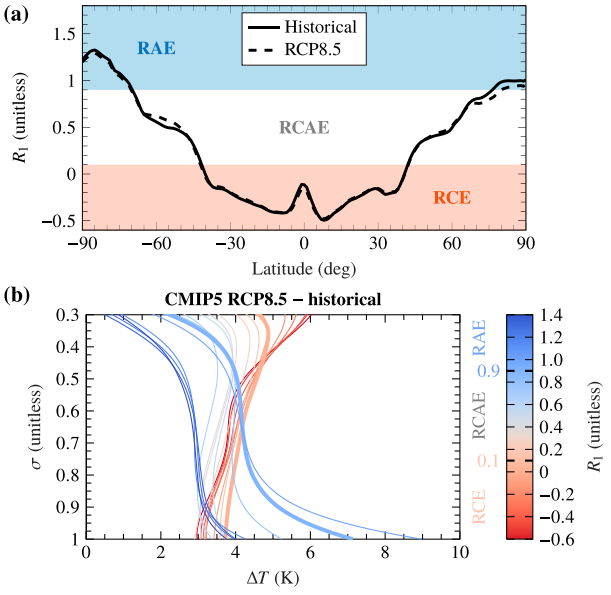

FIG. 12. (a) The zonal-mean, annual-mean structure of R_1 for the historical (solid black line) and RCP8.5 (dashed black line) CMIP5 multimodel mean. Orange, white, and blue regions indicate RCE, RCAE, and RAE, respectively. (b) The projected end-of-century temperature response to increased CO_2 binned by R_1 in the modern climate (bin widths are 0.1) for the CMIP5 multimodel mean. Thick blue and orange lines correspond to $R_1 = 0.9$ and $R_1 = 0.1$, respectively.

6. Summary and discussion

a. Summary

We quantified energy balance regimes in the modern climate, their link to lapse rate regimes, and their response to warming. We used the vertically integrated moist static energy

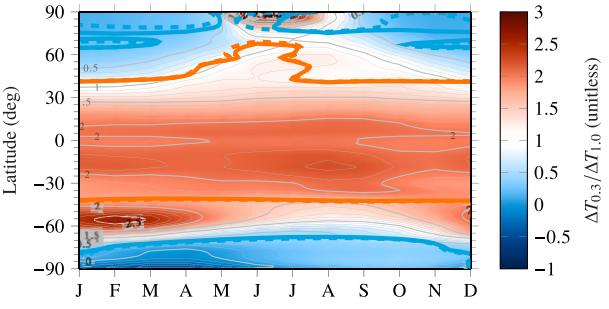

FIG. 13. The ratio of the temperature response to increased CO_2 in the upper troposphere ($\sigma = 0.3$) and the surface ($\sigma = 1.0$) are shown as filled contours (contour interval is 0.1) for the CMIP5 multimodel mean. The RCE/RCAE boundary is shown as a thick orange contour and the RAE/RCAE boundary is shown as a thick blue contour (solid for historical, dashed for RCP8.5).

budget to define a nondimensional number $R_1 = [\partial_t m + \partial_y(vm)]/R_a$ that quantifies regions of RCE ($R_1 \leq 0.1$), RAE ($R_1 \geq 0.9$), and RCAE ($0.1 < R_1 < 0.9$). In the annual mean, the RCE regime occurs equatorward of 40°, consistent with the occurrence of the moist adiabatic lapse rate regime. The RAE regime occurs poleward of 80°N and 70°S, consistent with the occurrence of the surface inversion lapse rate regime. Last, the RCAE regime occurs within 40°–70°S and 40°–80°N, consistent with the occurrence of the mixed lapse rate regime (more stable than a moist adiabat but does not exhibit a surface inversion).

Energy balance and lapse rate regimes in the modern climate exhibit weak seasonality in the Southern Hemisphere. In the Northern Hemisphere, regime transitions occur from RCAE to RCE in the midlatitudes and from RAE to RCAE in the high latitudes. The lapse rate also shows seasonal regime transitions in the northern middle and high latitudes, but there is a phase shift relative to the energy balance regime transition by 1–3 months. In the northern midlatitudes, this phase shift is associated with the seasonality of atmospheric storage.

A linear decomposition of the R_1 seasonality shows that the regime transition in the Northern Hemisphere midlatitudes is associated with the large seasonality of advection plus atmospheric storage. We hypothesized using an EBM that surface heat capacity controls the amplitude of advection plus storage and thus the seasonal regime transition in the northern midlatitudes. The hypothesis was confirmed by varying the mixed layer depth in aquaplanet simulations. As predicted by the EBM, aquaplanet simulations show that the amplitude of the R_1 seasonality increases as the mixed layer depth decreases. The midlatitude regime transition occurs for mixed layer depths less than 20 m in the aquaplanet. The phase of R_1 is also a function of the mixed layer depth in the aquaplanet, where the RCE regime transition occurs earlier in the season for shallower mixed layer depths. The importance of surface heat capacity on the seasonal amplitude of advection plus storage in the midlatitudes is consistent with Barpanda and Shaw (2020).

To understand the seasonality of energy balance regimes in the high latitudes, we tested the importance of sea ice for a polar ocean (Arctic) and topography for a polar continent (Antarctica) using mechanism-denial experiments. In the annual mean, the RAE regime only occurs over a polar ocean when thermodynamic sea ice is enabled. The energy balance regime seasonality depends on the seasonality of sea ice, which itself depends on the mixed layer depth in the aquaplanet. For shallower (25–40 m) mixed layer depths, RAE occurs from September to April when sea ice fraction, thickness, and surface albedo are large year-round. For deeper (45 and 50 m) mixed layer depths, RAE disappears in the fall when sea ice fraction, thickness, and surface albedo are small. Using the CESM experiments conducted by Hahn et al. (2020), we found that Antarctic topography alone cannot explain the lack of a high-latitude regime transition over Antarctica.

Finally, we showed that energy balance regimes in the modern climate can be used to interpret the vertical structure of the warming response in the annual mean, and seasonally in the tropics and the southern high latitudes. In the annual mean, regions of RCE in the modern climate that remain in RCE in the future exhibit amplified warming aloft. Regions of RAE in the modern climate that remain in RAE in the future exhibit amplified warming at the surface. Similar results hold seasonally in the tropics and the southern high latitudes. However, in the Northern Hemisphere middle and high latitudes, the seasonality of energy balance regimes in the modern climate is less directly related to the warming response due to the role of atmospheric heat storage in the midlatitudes and large changes in energy balance regimes in the Arctic.

TABLE B1. List of the 36 models that comprise the CMIP5 multimodel mean of the historical and RCP8.5 runs.

Models	
ACCESS1-0	GISS-E2-H-CC
ACCESS1-3	GISS-E2-R
BCC-CSM1-1	GISS-E2-R-CC
BCC-CSM1-1-m	HadGEM2-CC
BNU-ESM	HadGEM2-ES
CanESM2	INM-CM4
CCSM4	IPSL-CM5A-LR
CESM1-BGC	IPSL-CM5A-MR
CESM1-CAM5	IPSL-CM5B-LR
CMCC-CESM	MIROC5
CMCC-CM	MIROC-ESM
CNRM-CM5	MIROC-ESM-CHEM
CSIRO-Mk3-6-0	MPI-ESM-LR
FGOALS-g2	MPI-ESM-MR
GFDL-CM3	MRI-CGCM3
GFDL-ESM2G	MRI-ESM1
GFDL-ESM2M	NorESM1-M
GISS-E2-H	NorESM1-ME

b. Discussion

Our findings are consistent with Jakob et al. (2019), who showed that the tropics are close to RCE over large temporal (>5000 km) and spatial (>daily) time scales (achieved here through taking the zonal mean). Jakob et al. (2019) use the DSE budget to define RCE and primarily focus on the implications of the validity of RCE in the context of CRM configurations and convective aggregation in the tropics. Our work focuses on the nondimensional MSE budget, which has the advantage that it can be used as a more general criterion for

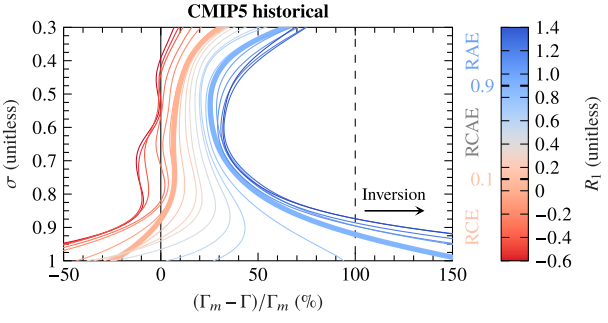

FIG. B1. As in Fig. 1, but for the CMIP5 historical multimodel mean.

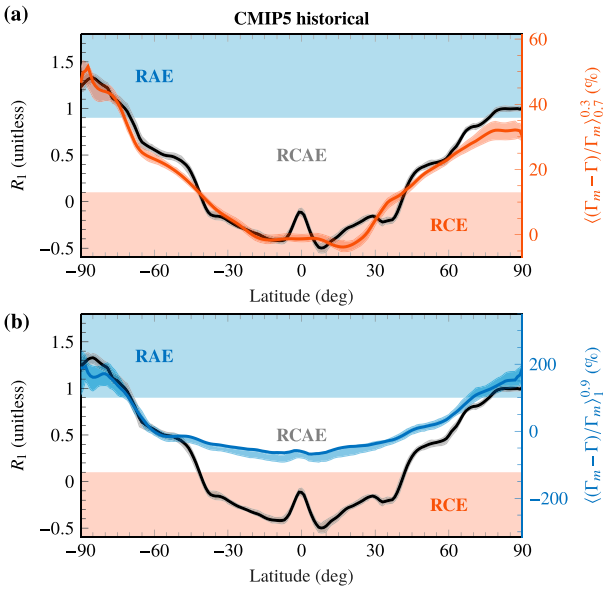

FIG. B2. As in Fig. 2, but for the CMIP5 historical multimodel mean. The shading indicates the interquartile range.

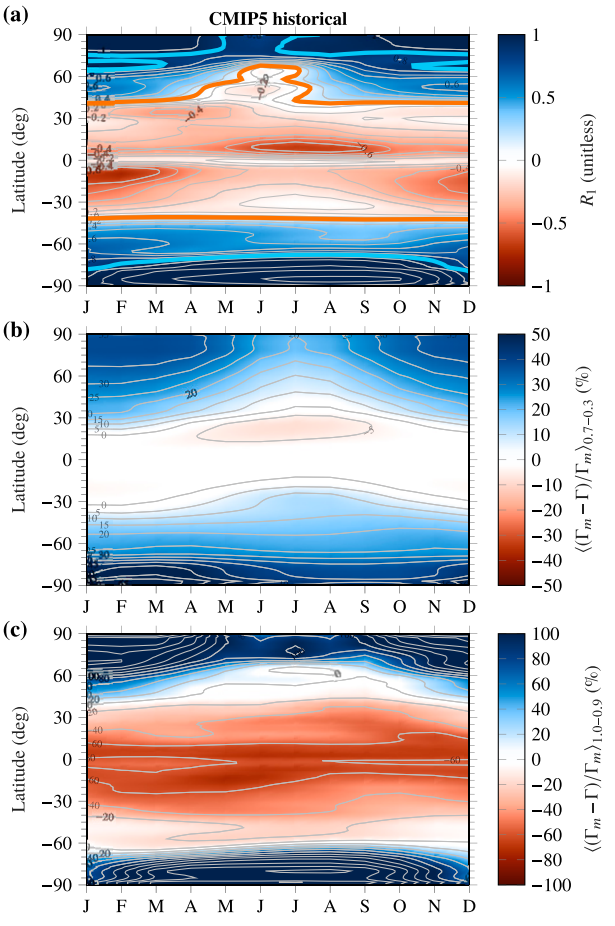

FIG. B3. As in Fig. 3, but for the CMIP5 historical multimodel mean.

defining energy balance regimes outside the tropics and in climates different from Earth's modern climate.

The energy balance regimes defined here were based on the vertically integrated MSE budget. The vertically integrated budget is useful, but it may have limitations when the vertical structure of advection, atmospheric storage, and radiation are important. For example, the discrepancy between the seasonality of energy balance and lapse rate regimes in the northern high latitudes may be related to different vertical structures of advection and atmospheric storage. Extending the RAE model of Cronin and Jansen (2016) to explicitly include atmospheric storage would be helpful for understanding the discrepancy.

While the mechanism-denial experiments involving sea ice show that sea ice is a necessary condition to reproduce the seasonality of energy balance regimes in the northern high latitudes, further experiments are necessary to 1) understand the discrepancy between the timing of energy balance and lapse rate regimes in the reanalysis data and 2) isolate the importance of the seasonally varying effective surface heat capacity and surface albedo effect of sea ice. Progress on goal 1 can be made by increasing the complexity of the sea ice representation (e.g., adding zonal asymmetry and/or sea ice dynamics) until the discrepancy in the timing of energy balance and lapse rate regimes can be reproduced. Progress on goal 2 can be made by running experiments with sea ice where the surface albedo is prescribed.

Our understanding of the southern high-latitude energy balance regime seasonality remains incomplete. In particular, experiments involving topography and a seasonally invariant high albedo were not successful in explaining the lack of a summertime regime transition in the southern high latitudes. Future work could test the sensitivity of the results to variations in surface albedo beyond the range explored here, the role of alternative mechanisms such as clouds and the large-scale circulation, or the confluence of multiple mechanisms.

The connection between energy balance regimes in the modern climate and the vertical structure of the global warming response demonstrated here using state-of-the-art GCMs complements the findings of Payne et al. (2015). However, a complete understanding of the latitudinal and seasonal structure of the vertical temperature response in the Northern Hemisphere middle and high latitudes and Southern Hemisphere midlatitudes requires further investigation. Previous studies showed that the vertical structure of the warming response in the RAE model is sensitive to the type of forcing (Payne et al. 2015; Cronin and Jansen 2016). Thus, decomposing the change in R_1 into dynamic and radiative components and investigating their link to the warming response may be a fruitful direction for future work.

The framework we introduced for quantifying energy balance regimes can be used to explore many interesting areas for future work. The framework can be extended to study the zonal structure of energy balance regimes. The role of zonal

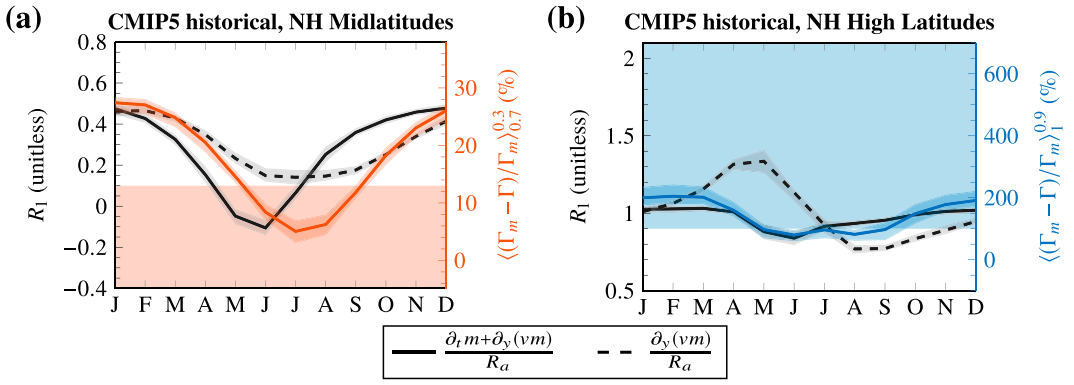

FIG. B4. As in Fig. 4, but for the CMIP5 historical multimodel mean. The shading indicates the interquartile range.

variations in surface heat capacity (land vs ocean) may be explored for the timing and amplitude of the Northern Hemisphere regime transitions. The framework can also be applied to quantify energy balance regime transitions in various paleoclimates. Previous studies suggest that high latitudes during warm epochs, such as the Eocene, may have been close to RCE (Abbot and Tziperman 2008) whereas RAE was more widespread during Snowball Earth (Pierrehumbert 2005). These are all exciting areas for future work.

Acknowledgments. The authors acknowledge support from the National Science Foundation (AGS-2033467). We thank Isaac Held, Nadir Jeevanjee, and one anonymous reviewer for their comments, which helped to improve the manuscript. We acknowledge the University of Chicago Research Computing Center for providing the computational resources used to carry out this work. We thank Lily Hahn for making the output of their CESM simulations publicly available.

Data availability statement. Data supporting this study are available through Knowledge@UChicago (https://knowledge.uchicago.edu/record/2925?ln=en). Additionally, ERA5 data are available through ECMWF (https://www.ecmwf.int/en/

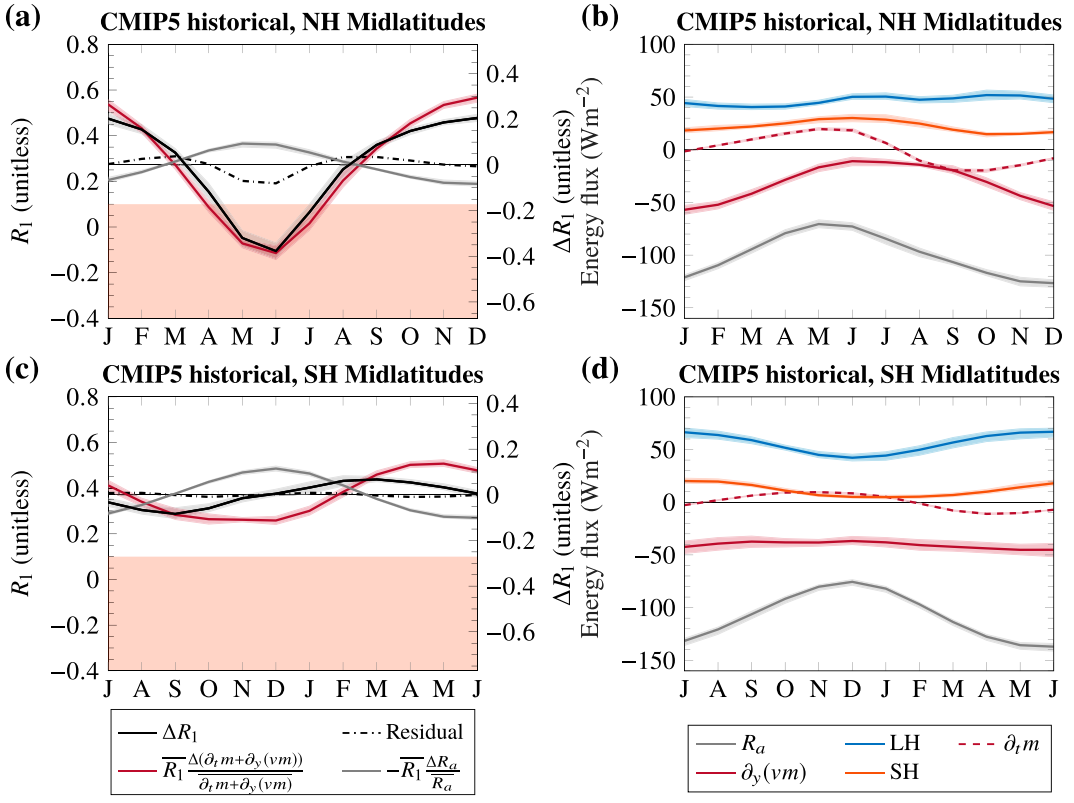

FIG. B5. As in Fig. 5, but for the CMIP5 historical multimodel mean. The shading indicates the interquartile range.

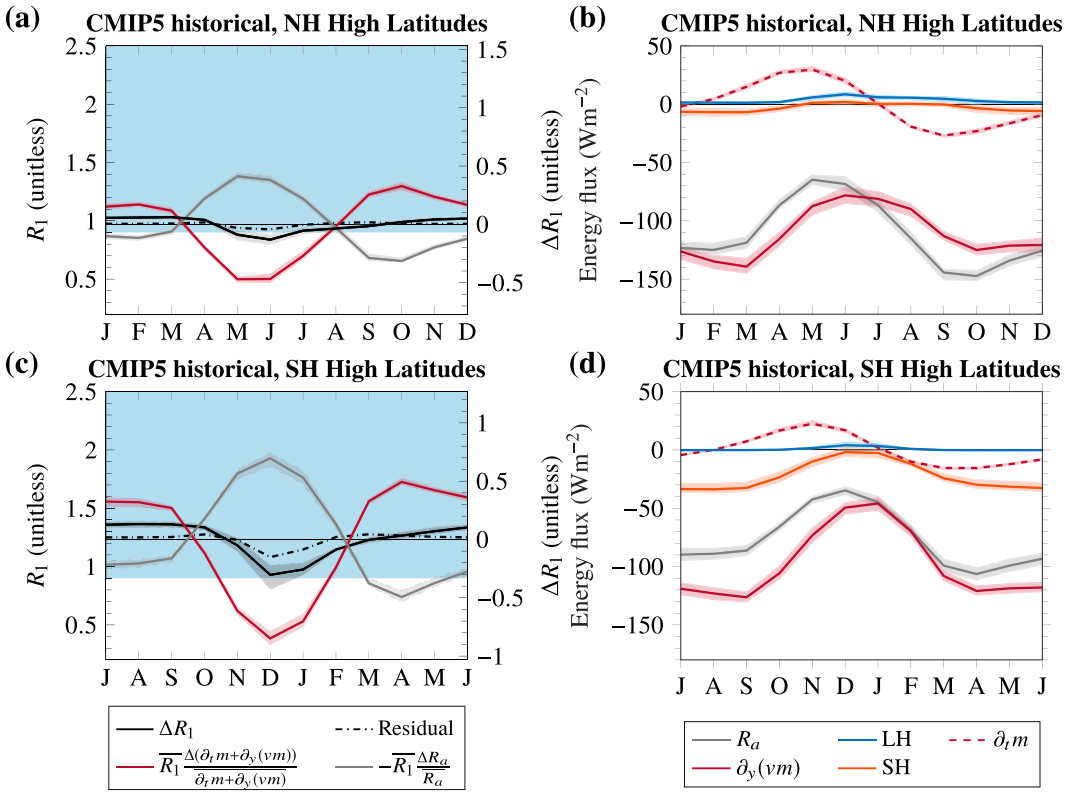

FIG. B6. As in Fig. 6, but for the CMIP5 historical multimodel mean. The shading indicates the interquartile range.

forecasts/datasets/reanalysis-datasets/era5). MERRA-2 data are available through NASA-GMAO (https://gmao.gsfc.nasa.gov/reanalysis/MERRA-2/). JRA-55 data are available through DIAS (https://jra.kishou.go.jp/JRA-55/index_en.html). CMIP5 data are available through ESGF (https://esgf-node.llnl.gov/projects/esgf-llnl/).

APPENDIX A

Lapse Rate Deviation from the Moist Adiabat

We use a centered finite difference of monthly pressure level temperature and geopotential data to compute the lapse rate and convert to sigma coordinates by masking out the data below surface pressure and taking a cubic spline interpolation. We perform this conversion for every latitude and longitude grid point. Following Stone and Carlson (1979), we define the deviation of the lapse rate from the moist adiabatic lapse rate as the fractional difference:

$$\delta_c = \frac{\Gamma_m - \Gamma}{\Gamma_m}, \tag{A1}$$

where Γ is the actual lapse rate in the reanalysis or GCM and Γ_m is the moist adiabatic lapse rate as defined in Eq. (3) in Stone and Carlson (1979).

APPENDIX B

Differences between the CMIP5 Historical Multimodel Mean and the Reanalysis Mean

In the reanalysis mean, there is a location of anomalously s table stratification between $\sigma = 0.9$ to 0.7 for $R_1 = 0$ (Fig. 1). This leads to a nonmonotonic relationship between the lapse rate deviation and R_1 in the vicinity of $\sigma = 0.8$. In comparison, for the CMIP5 multimodel mean (Table B1) the lower tropospheric stability does not show a pronounced peak and the lapse rate deviation is monotonic with respect to R1 (Fig. B1).

Both the reanalysis and CMIP5 multimodel mean agree on the seasonality of energy balance and lapse rate regimes in the low and middle latitudes (Figs. B2a, B3a,b, B4a, and B5).

In the high latitudes, the annual-mean surface inversion is stronger over Antarctica compared to the Arctic in the reanalysis mean (Fig. 2b). In comparison, the inversion strength exhibits small hemispheric asymmetry in the CMIP5 multimodel mean (Fig. B2b). Consistently, the near-surface lapse rate in the summertime Arctic is more stable in the CMIP5 multimodel mean (Figs. B3c and B4c).

In the reanalysis mean, there is a clear hemispheric asymmetry in the high-latitude R_1 seasonality (cf. Figs. 6a,c). In addition, there is a corresponding asymmetry in the

seasonality of the boundary layer lapse rate, where the lapse rate deviation in the northern high latitudes indicates that the inversion vanishes during summertime whereas the inversion persists year-round in the southern high latitudes (Fig. 3c). The asymmetry differs somewhat in the CMIP5 multimodel mean. Notably, R_1 exhibits stronger seasonality in the Southern Hemisphere and approaches the margin of the RCAE regime during summertime (cf. Figs. B6c and 6c). Consistent with an energy balance state on the margin of RCAE, the inversion vanishes in the southern high latitudes during summertime (Fig. B3c).

APPENDIX C

Deriving an Analytical Expression for ΔR_1 as a Function of Mixed Layer Depth

Following the Rose et al. (2017) EBM, we write the seasonality of TOA and SFC fluxes as a Fourier–Legendre series. Here we only consider the first harmonic as it is an order of magnitude larger than the second harmonic in the midlatitudes:

- $\Delta F_{\mathrm{TOA}} \approx a\Delta Q - B\Delta T_s$, where $a\Delta Q = Q^*\cos(\omega t)$; $\omega = 2\pi\ \mathrm{yr}^{-1}$, $Q^* = as_{11}Q_gP_1(\phi)$ is the amplitude of net TOA shortwave radiation, $s_{11} = -2\sin\beta$, where β is the obliquity, $P_1(\phi) = \sin\phi$, and $Q_g = 340\ \mathrm{W\ m^{-2}}$
- $\Delta T_s = T_s^*\cos(\omega t - \Phi)$, where T_s^* is the amplitude of surface temperature seasonality and Φ is the phase shift of ΔT_s relative to ΔQ; $T_s^* = Q^*\left[(B+2D)^2 + (\rho c_w d\omega)^2\right]^{-1/2}$ and $\Phi = \arctan[\rho c_w d\omega/(B+2D)]$ [see Rose et al. (2017) for the derivation of the analytical expression of surface temperature].

Using the results above, we can write Eq. (10) as

$$\Delta R_1 = \frac{1}{\overline{R}_a}\left[Q^*\cos(\omega t) - BT_s^*\cos(\omega t - \Phi) + \rho c_w d\omega T_s^*\sin(\omega t - \Phi)\right]. \tag{C1}$$

Substituting in T_s^* and Φ and simplifying, we obtain

$$\Delta R_1 = \frac{Q^*}{\overline{R}_a}\frac{2D}{(B+2D)^2 + (\rho c_w d\omega)^2}\left[(B+2D)\cos(\omega t) + \rho c_w d\omega\sin(\omega t)\right]. \tag{C2}$$

REFERENCES

Abbot, D. S., and E. Tziperman, 2008: Sea ice, high-latitude convection, and equable climates. *Geophys. Res. Lett.*, **35**, L03702, https://doi.org/10.1029/2007GL032286.

Andreas, E. L., C. A. Paulson, R. M. William, R. W. Lindsay, and J. A. Businger, 1979: The turbulent heat flux from Arctic leads. *Bound.-Layer Meteor.*, **17**, 57–91, https://doi.org/10.1007/BF00121937.

Barpanda, P., and T. A. Shaw, 2020: Surface fluxes modulate the seasonality of zonal-mean storm tracks. *J. Atmos. Sci.*, **77**, 753–779, https://doi.org/10.1175/JAS-D-19-0139.1.

Betts, A. K., 1982: Saturation point analysis of moist convective overturning. *J. Atmos. Sci.*, **39**, 1484–1505, https://doi.org/10.1175/1520-0469(1982)039<1484:SPAOMC>2.0.CO;2.

Bordoni, S., and T. Schneider, 2008: Monsoons as eddy-mediated regime transitions of the tropical overturning circulation. *Nat. Geosci.*, **1**, 515–519, https://doi.org/10.1038/ngeo248.

Bradley, R. S., F. T. Keimig, and H. F. Diaz, 1992: Climatology of surface-based inversions in the North American Arctic. *J. Geophys. Res.*, **97**, 15 699–15 712, https://doi.org/10.1029/92JD01451.

Cronin, T. W., and M. F. Jansen, 2016: Analytic radiative-advective equilibrium as a model for high-latitude climate. *Geophys. Res. Lett.*, **43**, 449–457, https://doi.org/10.1002/2015GL067172.

Devasthale, A., U. Willén, K.-G. Karlsson, and C. G. Jones, 2010: Quantifying the clear-sky temperature inversion frequency and strength over the Arctic Ocean during summer and winter seasons from AIRS profiles. *Atmos. Chem. Phys.*, **10**, 5565–5572, https://doi.org/10.5194/acp-10-5565-2010.

Donohoe, A., J. Marshall, D. Ferreira, and D. McGee, 2013: The relationship between ITCZ location and cross-equatorial atmospheric heat transport: From the seasonal cycle to the last glacial maximum. *J. Climate*, **26**, 3597–3618, https://doi.org/10.1175/JCLI-D-12-00467.1.

——, D. M. W. Frierson, and D. S. Battisti, 2014: The effect of ocean mixed layer depth on climate in slab ocean aquaplanet experiments. *Climate Dyn.*, **43**, 1041–1055, https://doi.org/10.1007/s00382-013-1843-4.

Gelaro, R., and Coauthors, 2017: The Modern-Era Retrospective Analysis for Research and Applications, version 2 (MERRA-2). *J. Climate*, **30**, 5419–5454, https://doi.org/10.1175/JCLI-D-16-0758.1.

Giorgetta, M. A., and Coauthors, 2013: The atmospheric general circulation model ECHAM6: Model description. MPI Rep. 135/2013 on Earth System Science, 172 pp., https://www.mpimet.mpg.de/fileadmin/publikationen/Reports/WEB_BzE_135.pdf.

Graham, R. M., and Coauthors, 2019: Evaluation of six atmospheric reanalyses over Arctic sea ice from winter to early summer. *J. Climate*, **32**, 4121–4143, https://doi.org/10.1175/JCLI-D-18-0643.1.

Hahn, L. C., K. C. Armour, D. S. Battisti, A. Donohoe, A. G. Pauling, and C. M. Bitz, 2020: Antarctic elevation drives hemispheric asymmetry in polar lapse rate climatology and feedback. *Geophys. Res. Lett.*, **47**, e2020GL088965, https://doi.org/10.1029/2020GL088965.

Hartmann, D., 2016: *Global Physical Climatology*. 2nd ed., Elsevier, 498 pp.

Held, I. M., 1993: Large-scale dynamics and global warming. *Bull. Amer. Meteor. Soc.*, **74**, 228–242, https://doi.org/10.1175/1520-0477(1993)074<0228:LSDAGW>2.0.CO;2.

Hersbach, H., and Coauthors, 2020: The ERA5 global reanalysis. *Quart. J. Roy. Meteor. Soc.*, **146**, 1999–2049, https://doi.org/10.1002/qj.3803.

Jakob, C., M. S. Singh, and L. Jungandreas, 2019: Radiative convective equilibrium and organized convection: An observational perspective. *J. Geophys. Res. Atmos.*, **124**, 5418–5430, https://doi.org/10.1029/2018JD030092.

Jeevanjee, N., and D. M. Romps, 2018: Mean precipitation change from a deepening troposphere. *Proc. Natl. Acad. Sci.*, **115**, 11 465–11 470, https://doi.org/10.1073/pnas.1720683115.

Kobayashi, S., and Coauthors, 2015: The JRA-55 reanalysis: General specifications and basic characteristics. *J. Meteor. Soc. Japan*, **93**, 5–48, https://doi.org/10.2151/jmsj.2015-001.

Korty, R. L., and T. Schneider, 2007: A climatology of the tropospheric thermal stratification using saturation potential vorticity. *J. Climate*, **20**, 5977–5991, https://doi.org/10.1175/2007JCLI1788.1.

Maykut, G. A., 1982: Large-scale heat exchange and ice production in the central Arctic. *J. Geophys. Res.*, **87**, 7971–7984, https://doi.org/10.1029/JC087iC10p07971.

Merlis, T. M., and I. M. Held, 2019: Aquaplanet simulations of tropical cyclones. *Curr. Climate Change Rep.*, **5**, 185–195, https://doi.org/10.1007/s40641-019-00133-y.

Nakamura, N., and A. H. Oort, 1988: Atmospheric heat budgets of the polar regions. *J. Geophys. Res.*, **93**, 9510–9524, https://doi.org/10.1029/JD093iD08p09510.

Neelin, J. D., and I. M. Held, 1987: Modeling tropical convergence based on the moist static energy budget. *Mon. Wea. Rev.*, **115**, 3–12, https://doi.org/10.1175/1520-0493(1987)115<0003:MTCBOT>2.0.CO;2.

Payne, A. E., M. F. Jansen, and T. W. Cronin, 2015: Conceptual model analysis of the influence of temperature feedbacks on polar amplification. *Geophys. Res. Lett.*, **42**, 9561–9570, https://doi.org/10.1002/2015GL065889.

Pendergrass, A. G., K. A. Reed, and B. Medeiros, 2016: The link between extreme precipitation and convective organization in a warming climate: Global radiative-convective equilibrium simulations. *Geophys. Res. Lett.*, **43**, 11 445–11 452, https://doi.org/10.1002/2016GL071285.

Pierrehumbert, R. T., 2005: Climate dynamics of a hard snowball Earth. *J. Geophys. Res.*, **110**, D01111, https://doi.org/10.1029/2004JD005162.

Popke, D., B. Stevens, and A. Voigt, 2013: Climate and climate change in a radiative-convective equilibrium version of ECHAM6. *J. Adv. Model. Earth Syst.*, **5** (1), 1–14, https://doi.org/10.1029/2012MS000191.

Porter, D. F., J. J. Cassano, M. C. Serreze, and D. N. Kindig, 2010: New estimates of the large-scale Arctic atmospheric energy budget. *J. Geophys. Res.*, **115**, D08108, https://doi.org/10.1029/2009JD012653.

Riehl, H., and J. S. Malkus, 1958: On the heat balance of the equatorial trough zone. *Geophysica*, **6**, 503–538.

Roberts, C. D., M. D. Palmer, R. P. Allan, D. G. Desbruyeres, P. Hyder, C. Liu, and D. Smith, 2017: Surface flux and ocean heat transport convergence contributions to seasonal and interannual variations of ocean heat content. *J. Geophys. Res. Oceans*, **122**, 726–744, https://doi.org/10.1002/2016JC012278.

Romps, D. M., 2011: Response of tropical precipitation to global warming. *J. Atmos. Sci.*, **68**, 123–138, https://doi.org/10.1175/2010JAS3542.1.

Rose, B. E. J., T. W. Cronin, and C. M. Bitz, 2017: Ice caps and ice belts: The effects of obliquity on ice-albedo feedback. *Astrophys. J.*, **846**, 28, https://doi.org/10.3847/1538-4357/aa8306.

Shaw, T. A., and R. J. Graham, 2020: Hydrological cycle changes explain weak Snowball Earth storm track despite increased surface baroclinicity. *Geophys. Res. Lett.*, **47**, e2020GL089866, https://doi.org/10.1029/2020GL089866.

Stevens, B., et al., 2013: Atmospheric component of the MPI-M Earth system model: ECHAM6. *J. Adv. Model. Earth Syst.*, **5**, 146–172, https://doi.org/10.1002/jame.20015.

Stone, P. H., and J. H. Carlson, 1979: Atmospheric lapse rate regimes and their parameterization. *J. Atmos. Sci.*, **36**, 415–423, https//doi.org/10.1175/1520-0469(1979)036<0415:ALRRAT>2.0.CO;2.

Tastula, E.-M., T. Vihma, E. L. Andreas, and B. Galperin, 2013: Validation of the diurnal cycles in atmospheric reanalyses over Antarctic sea ice. *J. Geophys. Res. Atmos.*, **118**, 4194–4204, https://doi.org/10.1002/jgrd.50336.

Taylor, K. E., R. J. Stouffer, and G. A. Meehl, 2012: An overview of CMIP5 and the experiment design. *Bull. Amer. Meteor. Soc.*, **93**, 485–498, https://doi.org/10.1175/BAMS-D-11-00094.1.

Tjernström, M., and R. G. Graversen, 2009: The vertical structure of the lower Arctic troposphere analysed from observations and the ERA-40 reanalysis. *Quart. J. Roy. Meteor. Soc.*, **135**, 431–443, https://doi.org/10.1002/qj.380.

Warren, R. A., M. S. Singh, and C. Jakob, 2020: Simulations of radiative-convective-dynamical equilibrium. *J. Adv. Model. Earth Syst.*, **12**, e2019MS001734, https://doi.org/10.1029/2019MS001734.

Williams, E., and N. Renno, 1993: An analysis of the conditional instability of the tropical atmosphere. *Mon. Wea. Rev.*, **121**, 21–36, https://doi.org/10.1175/1520-0493(1993)121<0021:AAOTCI>2.0.CO;2.

Wing, A. A., K. A. Reed, M. Satoh, B. Stevens, S. Bony, and T. Ohno, 2018: Radiative–Convective Equilibrium Model Intercomparison Project. *Geosci. Model Dev.*, **11**, 793–813, https://doi.org/10.5194/gmd-11-793-2018.

Xu, K.-M., and K. A. Emanuel, 1989: Is the tropical atmosphere conditionally unstable? *Mon. Wea. Rev.*, **117**, 1471–1479, https://doi.org/10.1175/1520-0493(1989)117<1471:ITTACU>2.0.CO;2.

Zhang, Y., D. J. Seidel, J.-C. Golaz, C. Deser, and R. A. Tomas, 2011: Climatological characteristics of Arctic and Antarctic surface-based inversions. *J. Climate*, **24**, 5167–5186, https://doi.org/10.1175/2011JCLI4004.1.